Microfracturing during primary migration in shales

Marcello Goulart Teixeira, Frédéric Donzé, François Renard, Hamed Panahi, Efthymios Papachristos, Luc Scholtès

Microfracturing during primary migration in shales

Marcello Goulart Teixeira[1], Frédéric Donzé[2], François Renard[3,4,*], Hamed Panahi[3], Efthymios Papachristos[2] and Luc Scholtès[5]

[1]*Departamento de Ciência da Computação, Federal University of Rio de Janeiro, Brazil*

[2]*Univ. Grenoble Alpes, 3SR, CS 40700, F-38058, Grenoble cedex 9, France*

[3]*Departments of Geosciences and Physics, Physics of Geological Processes, University of Oslo, Norway*

[4]*Univ. Grenoble Alpes, ISTerre, CS 40700, F-38058, Grenoble cedex 9, France*

[5]*Univ. de Lorraine & CNRS & CREGU, Laboratoire GeoRessources, Nancy, France*

* Corresponding author: francois.renard@univ-grenoble-alpes.fr

Abstract

In several geological environments, chemical reactions are coupled to rock deformation and the associated stresses induced locally interact with the far field loading. This is the case in immature shales that undergo burial and diagenesis, where the organic matter evolves with temperature into hydrocarbons which induces local volume expansion. At large scale, this mechanism is responsible for the transport of hydrocarbons from source to reservoir rocks, a process referred to as primary migration. However, how the interactions between local fluid production, microfracturing, and transport are coupled remain to be understood. Here, we analyze this coupling phenomenon by developing a discrete element model where the generation of local overpressures occurring in kerogen patches is simulated, while the surrounding rock is subjected to external loading. It is shown that, due to local fluid overpressure; microfracturing occurs and brings the fluids to migrate through the medium. The numerical results are confirmed by laboratory experiments where the network of microfractures induced in an immature Green River shale sample heated under small differential stress was imaged in three dimensions using X-ray microtomography. Moreover, the numerical simulations identify that the state of differential stress and the initial kerogen distribution constitute two key parameters that control the formation of the three-dimensional percolating microfracture network and could thus explain primary migration in shale rocks.

Keywords: shale, microfracture, kerogen, X-ray tomography, Discrete Element Model

Highlights

- Kerogen maturation produces microfractures in shale rocks

- Microfractures form a percolating network

- Differential stress and spatial distribution of kerogen control the geometry of the final microfractures network

1. Introduction

The coupled response of chemical reactions and deformation in rocks can induce the development of localized damage in the form of connected microfractures or microporosity which facilitate the circulation of fluids. These phenomena are observed in various geological processes such as weathering and erosion of surface rocks (Røyne et al., 2008; Jamtveit and Hammer, 2012), hydration of the Earth's lower crust (Peacock, 1993; Jamtveit et al., 2000), dehydration of sediments in subduction zones (Ulmer and Trommsdorff, 1995; Saffer and Bekins, 1998; Brantut et al., 2012), alteration of monuments by salt precipitation (Noiriel et al., 2010), or the maturation of organic matter in source rock sediments (Snarsky, 1961; Tissot and Welte, 1978; England et al., 1987; Hunt, 1990; Lafargue et al., 1993, 1998; Vernik, 1994; Rudkiewicz et al., 1994; Kobchenko et al., 2011). For the latter, the coupling between maturation of the organic matter and creation of porosity by fracturing of the source rocks during burial may lead to hydrocarbon escape towards a more porous reservoir, a process called primary migration.

Shale rocks overlie or underlie most hydrocarbon-bearing reservoirs, forming cap rocks and source rocks. They prevent fluids from escaping due to their low permeability and by a capillary sealing mechanism controlled by the small pores (Horsrud et al., 1998). While the presence of fractures in shales in outcrops and from cores through unconventional reservoirs has been

described (Gale et al., 2014), the presence of microfractures and microporosity at smaller scales, that may control the overall permeability, is debated because of scarce observations (Gale et al., 2014; Kalani et al., 2015, Ougier-Simonin et al., 2016). Sometimes, bitumen-filled microfractures with chemical characteristics similar to decomposed kerogen are observed (Lash and Engelder, 2005), in other cases the presence of sealed veins indicate that microfractures were open at depth (Kalani et al., 2015). Moreover, microfractures control the long-term sealing capacities of cap rocks, the expulsion of hydrocarbon during primary migration, and the potential increase in permeability when reactivated by hydraulic fracturing. More generally, the petrophysical properties of argillite rocks have fundamental implications, for example on their frictional behavior in faults (Brantut et al., 2008) and in controlling their permeability (Holland et al., 2006).

Kerogen maturation into oil and gas leads to a volume increase in the order of 10-20% at standard pressure and temperature conditions. In many cases maturation takes place within the internal porosity of kerogen flakes, which may indicate that expansion of the solid might be another cause of microfracturing. Such overpressure mechanisms have been proposed to be high enough to fracture the source rock (Pelet and Tissot, 1971; Vernik, 1994). When the overpressure reaches a critical stress, microfractures starts to nucleate and propagate (Hunt, 1990; Capuano, 1993; Vernik, 1994; Jin et al., 2010). Propagating microfractures may then coalesce and even get connected to pre-existing vertical fractures which would further facilitate hydrocarbon primary migration (Fan et al., 2012).

Here, we study the process of primary migration coupled to microfracture development by a combined experimental and numerical approach. The experimental component involves imaging in three dimensions (X-ray tomography) of Green River shale samples that were heated under small differential stress, in order to characterize the network of microfractures produced during the maturation of organic matter (Kobchenko et al., 2011; Panahi et al., 2013). The natural Green River shale rock contains kerogen organic matter which is present in the form of sub-millimeter elongated ellipsoids distributed in the rock matrix. These patches, when undergoing thermal maturation, act as local sources of overpressure due to the breakage of shorter molecules from the very long chained molecules constituting the polymerized kerogen. Such pressure variations can induce local microfracturing at the scale of the kerogen patches. These fractures then grow and ultimately connect to each other in three-dimensions, spanning the whole volume of the rock mass. In order to gain more insight into the process, we simulate

numerically the formation and propagation of these microfractures at the scale of kerogen patches using a three dimensional model based on the discrete element method (Cundall and Strack, 1979, Donzé and Magnier, 1993). The conditions under which these microfractures become the preferred paths for fluid products and control primary migration are then discussed.

2. Materials and methods

2.1 Experiments of shale maturation

Two core samples of a Green River shale, that contains 5 wt. % type I kerogen, were heated to 390°C in pressure vessels for 48 hours to transform the kerogen into oil and gas. The rock is made of quartz, clays, pyrite, and carbonate minerals and has a low porosity, close to 5% as measured by helium gas adsorption method. This rock is an immature shale and previous experiments have shown that kerogen maturation at atmospheric pressure can be performed at temperatures in the range 300-400°C (Kobchenko et al., 2011; Panahi et al., 2013). The samples, 25 mm diameter and height, were cored perpendicularly to bedding. The kerogen is organized into small elongated patches, 10-200 micrometers long and 2-5 micrometers thick, spread along preferential beds in the shale. The microstructure of the rock was imaged before heating using high resolution X-ray microtomography at beamline ID19 at the European Synchrotron Radiation Facility (Grenoble, France), at a voxel size of 0.16 micrometer, allowing identification of the 3D geometry of kerogen patches (Figure 1).

A steel sample holder was custom-made to contain the sample and simulated a moderate confinement. Some holes were drilled into the holder to enable the fluids released during experiments to escape. A wave spring was used to apply an axial load to the samples, while the vessel was pressurized at 10 bars with nitrogen gas. The sample was not jacketed and a small differential state of stress was applied to the samples by the wave spring that applied a force on the top surface of the sample, equivalent to an axial stress of 12 bars. The present experiments did not reproduce the whole maturation process at conditions of several kilometers depth in sedimentary basins. Rather, the main motivation was to show that the presence of a small differential stress can explain the formation of a connected 3D network of microfractures. We observed that the organic matter transformed into oil, as observed by some hydrocarbon stains released in the pressure vessel and around the rock samples after the experiments. Moreover, visible fractures could be seen on the outer surface of each sample, which were imaged in 3D

using a laboratory X-ray microtomograph with a voxel size of 11 micrometers. The 3D volumes were processed using the software AvizoFire™ to visualize the fractures.

2. 2 Numerical simulation of shale maturation

Numerical modeling was used to evaluate the possible mechanisms of kerogen maturation-induced microfracturing. In particular, the discrete element method (DEM) was chosen because of its capability to simulate the propagation of fractures within a rock matrix containing pre-existing heterogeneities such as bedding and varying kerogen concentration along laminations (Scholtès and Donzé, 2012). For instance, this method has already been used for the analysis of rock failure mechanisms involving wing crack propagation (Duriez et al., 2016), fractures coalescence (Scholtès and Donzé, 2012) or even hydrofracture propagation (Papachristos et al., 2016).

The simulations were performed with the YADE Open DEM platform (Kozicki and Donzé, 2008, Kozicki and Donzé, 2009; Smilauer et al., 2015), where the solid phase is represented by a discrete element packing whose respective motion is ruled by Newton's second law and the fluid flow is simulated using a finite volume method (Catalano et al., 2014). Regarding the mechanical behavior of the model, each interaction force linking the discrete elements obeys an elastic-brittle behavior in both normal and tangential directions. Under stress or strain loading, the bonds can break by either tensile or shear failure mechanism, following a modified Mohr-Coulomb criterion with a tension cut-off (for details, see Scholtès and Donzé, 2013). The fluid flows through an interconnected pore network located in between the discrete elements (dual space). The DEM and finite volume methods are fully coupled in the sense that any deformation of the solid phase affects the fluid flow and, conversely, any variation in pore pressure induces deformation of the medium (Papachristos et al., 2016). The local interporal fluid conductance k is formulated in order to capture the high permeability contrast between the fractures and the intact rock matrix (Figure 2a). The conductance of the throats connecting the pores located in the intact rock matrix is computed as proposed by Chareyre (2012). While fractures form, i.e. when broken bonds are identified in the model, the corresponding pore throat is replaced by a parallel plate model and the flow governed by the cubic law. k is then computed as a function of the fracture aperture which is updated at each time step of the simulation (Papachristos et al., 2016).

We choose here to model a tight rock with petrophysics parameters typical of a shale located at 5 km depth (Sone and Zoback, 2013), and a fluid with properties (viscosity and bulk modulus) similar to that of water. Table 1 shows the values of the parameters used to model the problem (Abousleiman et al., 2008). We consider a 26 mm size cubic sample, represented by a dense packing constituted of 10000 discrete elements (Figure 2b). The system is isothermal and heat exchanges are not considered.

The microstructure of the numerical samples takes into account two observations (Figure 1). Some layers at the millimeter scale are kerogen-rich, and the kerogen is organized into ellipsoidal patches, i.e. a set of pre-existing heterogeneities considered as initial fractures in the model. As a result, we designed a synthetic shale sample that contains layers and ellipsoidal patches of organic matter (Figure 2c). The number of kerogen patches (1, 2, or 13), their persistences (parameter $p=d/D$ in Figure 3), and relative positions in the kerogen-rich layers are varied. Here, the persistence p is a dimensionless geometric parameter that represents the ratio between the diameter d of kerogen patches and the distance D between the centers of two neighboring patches. To simulate kerogen maturation, the fluid pressure is increased progressively in each pre-existing kerogen patches by imposing a constant flow rate at their centres. As a result of the pressure buildup, fracturing occurs along the kerogen-matrix interface (at the tips of the kerogen patches), driving the fluid to propagate into the low permeable rock matrix before escaping freely outside the sample (a fluid pressure of 0 Pa is imposed at its boundaries). In addition, the sample can be confined under isostatic external stress with $\sigma_h = \sigma_H = \sigma_v = 80$ MPa or under differential stress state with $\sigma_h = \sigma_H = 80$ MPa, while σ_v can be varied between 90 and 110 MPa. Here, $\sigma_h = \sigma_H$ are the two main horizontal stresses and σ_v is the vertical stress applied on the sample's boundaries (Figure 2b).

In the present study, the experiments are used to illustrate the physical process of fluid expulsion during kerogen maturation and the numerical simulations are performed to explore a range of parameters rather than reproduce directly the experiments. For this reason the choice of geometrical parameters for the simulations is a compromise between comparing simulation results with the specific Green River shale used in the experiments and providing a physical understanding of the control parameters of fluid expulsion during kerogen maturation. In the simulations, the size of the sample is centimeter scale (Figure 3), as in the experiments (Figure 4a), and the ratio between the kerogen patch diameter and the distance between the centers of two kerogen patches, which is referred to as the persistence, is similar as well. However, to be

able to characterize the effect of individual kerogen patches, we have chosen dimensions of kerogen patches larger in the numerical simulations (several millimeters) than in the natural Green River shale (several hundred micrometers).

Simulations were performed by varying from one, two, up to thirteen the number of kerogen patches as well as their size in the numerical sample. With one patch, the propagation of a single fracture can be modelled. With two kerogen patches, local stress and progressive failure interactions are studied when both fractures propagate simultaneously. With thirteen initial kerogen patches, orientation and connectivity trends occurring during microfracturing can be observed. This geometry is used to upscale from single kerogen patch to the microfracturing of the whole rock, taking into account the interaction process between several fractures, which has been neglected in previous works (e.g. Lash and Engelder, 2005; Zhang et al. 2008). In the simulations with one or two kerogen patches, the diameter d of the patch was set to a value of 6 mm. The horizontal offset L between the patches was varied between 0 and ±2 mm for simulations with two patches.

In the simulations with thirteen kerogen sources, the patches are located in three different layers with 4, 5 and 4 patches located at 7, 13, and 19 mm from the bottom in the vertical direction, respectively (Figure 3). In addition, the patch diameter d was varied between 1, 4, 6, and 7 mm, corresponding to a persistence p of 0.12, 0.47, 0.71 and 0.83, respectively, p being defined by $p = d / D$, with D = 8.5 mm, the distance between the center of the kerogen patches. The value d = 6 mm was chosen such that the total surface area of the kerogen in the intermediate layer is equal to 20% of the section area of the kerogen-rich bed in that sample. The present simulations could be rescaled for smaller size kerogen patches and smaller rock volumes, as those observed in the tomography data of the Green River shale samples where d and D are ten to fifty times smaller, whereas the persistence p is the same as in the numerical simulations.

3. Results

3.1 Experiments of shale maturation

The maturation of Green River shale samples to temperatures up to 390°C was previously studied time-lapse during heating (Kobchenko et al., 2011; Panahi et al., 2013) and it was shown that fractures developed parallel to bedding in absence of confining stress and differential stress. Here, a small axial differential stress of 12 bars is applied to the sample, and under the effect of

heating hydrocarbon is produced, as suggested by the presence of stains of oil on the sample after maturation (Figure 4a). Using X-ray microtomography imaging, the microstructure of the fractured shale becomes clearly visible. Most of the microfractures are horizontal (Figure 4c-d) and parallel to the bedding. They have formed presumably by the lateral propagation of fractures initiating off kerogen patches (Figure 4b), due to local overpressure build-up during kerogen maturation. Interestingly, several fractures are also oriented vertically. The maturation process under a small differential stress allows the formation of a fracture network that percolates in three-dimensions across the whole volume, allowing the fluid to freely escape (Figure 4c-e). The main difference with previous studies for which no differential was applied (Kobchenko et al., 2011; Panahi et al., 2013) is that here both horizontal and vertical microfractures could develop, creating a connected network in three dimensions. To summarize, axial differential stress favors vertical growth whereas bedding anisotropy favors horizontal growth.

3.2 Numerical simulations

Under an increase of local pressure in the kerogen patches, fluid escapes by breaking interparticle cohesive bonds and thus creating damage (i.e. microfractures) inside the rock matrix. To quantify this damage and the associated fluid migration, we calculate the value of the parameter P_{32} that represents the intensity of the fractures, i.e. the total surface of the fractures divided by the total volume of the numerical sample (Papachristos et al., 2016) and that is defined as:

$$P_{32} = \frac{\sum_i A_i}{V} \quad (1)$$

with A_i the surface area of the ith microfracture, and V the initial volume of the sample.

The orientation of hydraulically induced microfractures is quantified by defining the dip angle θ, i.e. the angle between the vector normal to the microfracture surface and the vertical axis of the sample. If only horizontal fractures are present, the angles θ cluster around 0°; whereas in case of vertical fractures, θ reaches 90°. Finally, the vertical interconnectivity of the microfractures is expressed using a fracture layer ratio of damage in kerogen-free and kerogen-rich layers, which is characterized through the parameter K defined as:

$$K = \frac{NK}{WK} \quad (2)$$

with *NK* the quantity of microfractures in kerogen-free layers (*No Kerogen*), and *WK* the quantity of microfractures in kerogen-rich layers (*With Kerogen*) (Figure 5). *NK* and *WK* represent the values of P_{32} (Equation 1) in both layers. In the following sections, the main results of the simulations are presented.

3.2.1 Damage around a single kerogen patch

Here, we consider a patch of kerogen with a diameter d = 6 mm, located at the center of the sample, where fluid pressure is increased with time. Four simulations were performed where the vertical compressive stress σ_v was varied between 80 and 110 MPa, while the horizontal stresses were maintained constant and equal to 80 MPa. A vertical section is made through the middle of the numerical sample (Figure 6), where the red discs represent the newly created microfractures propagating from the initial horizontal kerogen patch and where fluid migration is highlighted by the dark cells of the finite volume mesh. Microfractures nucleate at the tip of the initial kerogen patch, before propagating away. For a hydrostatic stress state loading, the resulting fracture composed of the connected microfractures stays in the plane of the source fracture, as observed in experiments (Kobchenko et al., 2011). A different behavior can be observed for a differential stress state of 20 MPa where the microfractures tend to rotate towards the direction of maximum compressive stress σ_v and grow initially at an angle of 30° with the vertical direction. Away from the initial source fracture, these microfractures tend to become aligned with the vertical direction. As a consequence, fluid also tends to migrate along the direction of maximum stress where fractures open under the application of a differential stress as usually found in sedimentary basin. Moreover, the amount of microfracturing measured by the parameter P_{32} (Figure 7b) shows a slight linear decrease as the vertical stress increases, whereas the ratio of microfractures in kerogen-free compared to kerogen-rich layers increases with increasing vertical stress (Figure 7a). The decrease of P_{32} with increasing vertical stress is due to the fact that, at the onset of microfracturing, a higher overpressure in the kerogen patch is necessary to fracture the matrix around when the external stress is increased. Moreover, increasing the differential stress enhances the localization of the deformation into a narrower damage zone, whose propagation path follows more directly the direction of the main compressive stress. The increase of *K*, which is about one order of magnitude, shows that, besides the re-alignment of the microfractures with the maximum stress, an important spatial

reorganization of the microfractures network takes place under a state of differential stress, which enhances the interlayer connectivity.

3.2.2 Damage around two kerogen patches

In these simulations, one kerogen patch is located 10 mm above the bottom of the sample and the second patch at 16 mm. The relative position, i.e., the horizontal distance L between the kerogen patches is varied between $-2r$, $-r$, 0, r and $2r$, where r is the radius of the patch equal to 3 mm in these simulations, and the minus sign represents the vertical superposition of the initial fractures (Figure 8). The vertical stress σ_v is varied between 80 and 100 MPa.

The damage due to kerogen maturation and fluid migration evolves spatially under the influence of both the imposed external stress and the local stress field generated by the pressure increase in each kerogen patch, allowing stress interactions depending on the relative position of the two patches (Figure 8). There is a clear effect on damage pattern from both parameters. When the two kerogen patches tips are vertically aligned (Figures 8a, 8c), the stress interaction is at its maximum (Jiang et al., 1991) and contributes to increase the vertical connectivity by a coalescence process. Note that, in the case of vertically aligned kerogen patches (Figures 8d), the dilatancy due to the over-pressurized fluid also increases the compressive stress in between the patches, leading to a strong fracture interaction (Papachristos et al., 2016). When the two kerogen patches are separated by too large a distance ($r > 2$ mm), no stress interaction could be seen, limiting therefore the inter-layer connectivity (Figure 9).

The increase of the vertical differential stress enhances the rotation of microfractures toward the direction of the maximum principal stress, allowing a faster coalescence between the damage zones (Figure 8c). This is also clearly measured from the total surface area of the microfractures (P_{32}), which is greater when the vertical compressive stress is larger. We also show below that this parameter P32 increases even more with increasing differential stress when more than two kerogen patches are present, demonstrating the importance of local interactions between several sources of overpressure.

3.2.3 Damage with thirteen kerogen patches

In these simulations, a larger number of kerogen patches (thirteen) are inserted into the shale model. This geometry is closer to what can be observed in a natural sample. The patches are located in three layers (Figure 3). The patch diameters are varied between 1-7 mm,

corresponding to a persistence p in the range 0.12-0.83. The external vertical compressive stress is varied in the range 80-110 MPa, for constant horizontal stresses equal to 80 MPa.

The influence of the vertical stress on microfractures development is presented in Figure 10 where a vertical slice is made through the center of the volume as illustrated on Figure 3. Similar to the results shown in Figures 6 and 8 for a smaller number of kerogen patches, the local maximum stress (Figure 10a) tends to align with the maximum applied stress direction (Figure 10b). According to this reorientation, it can be observed once again that the distribution of generated microfractures is strongly affected by the existence of the differential stress. A systematic analysis of the orientation of the newly formed microfractures is shown on Figure 11. There is a clear effect of the imposed external stress: the microfractures tend to rotate preferentially towards the vertical axis as σ_v increases. For intermediate values of σ_v, the rose diagrams show that the microfractures are oriented in all directions, favoring a 3D network. At low differential stress most of them are horizontal (the initial kerogen microstructure dominates), whereas at high differential stress most of them are vertical (the external loading dominates).

The effect of persistence p (see Figure 3) on the intensity and spatial distribution of the microfractures is presented in Figure 12. The evolution of the relative value of the ratio K shows a strong non-linearity as the differential stress becomes important, as can be expected during an extensive tectonic episode (Figure 12a). In the case of highly persistent kerogen patches ($p >$ 0.71 in Figure 12b), the amount of new microfractures does not need to massively increase to connect the different patches, and the microfracture intensity values remain low. However, it can be seen that the increase of the differential stress remains of secondary effect on the evolution of the microfracture intensity (Figure 12b).

4. Discussion

4.1 Microfractures in shales

Several studies have been performed to address microfracturing in tight rocks because natural fractures in shales play a role in controlling cap rock integrity. They focused on technologies related to underground nuclear waste disposal and, more recently, geological storage of CO_2 (e.g. Bolton et al., 2000; Yang and Aplin, 2007; Sarout and Guéguen, 2008; Ababou *et al.*, 2011; Skurtveit *et al.*, 2012; Ghayaza *et al.*, 2013). Open microfractures from the nanometer to

332 micrometer scale affect the physical properties of rocks, such as compressibility, strength,
333 elastic wave velocities, and permeability (Kranz, 1983). The fluid transport properties of low-
334 permeability rocks are primarily controlled by the structure of available flow pathways (Keller
335 et al., 2011) such as microfractures, the rock matrix having much lower permeability and high
336 capillary entry pressure. Microfractures also control the long-term sealing capacities of cap-
337 rocks and the expulsion of hydrocarbons during primary migration. In this case, the fluid which
338 escapes due to mechanical compaction or generation of hydrocarbons is determined by the
339 width and spacing of the fractures. As the effective stress in the cap-rock changes, because of
340 increasing fluid pressure in the underlying reservoir, fractures may be created and/or
341 reactivated, and they may close when the fluid pressure in the reservoir decreases because of
342 loss of fluid through the fractures. It is particularly important to understand and characterize
343 these properties in deep reservoirs, for which exploration and production boreholes are
344 particularly costly.

345 Several processes contribute to microfracture formation in borehole cores and in outcrop
346 samples (Vernik 1994; Dewhurst et al., 2011). Some of these occur during sample recovery or
347 exhumation and unloading, while others occur naturally at depth. Actually, two types of
348 microfracture orientations can be identified in shales. The first type is oriented parallel to the
349 bedding, along planes of weakness, and the second type, oriented at high angles relative to the
350 first, may intersect the first to form a 3D network that greatly increases the permeability and
351 reduces the capillary entry pressure in the vertical direction (Breyer, 2012; Padin et al., 2014;
352 Kalani et al., 2015). The existence of these two types of microfractures is a necessary, but not
353 sufficient, condition for the formation of a percolating microfracture network at the decimeter
354 to meter scale. In the present study, we characterize how hydrocarbon maturation can lead to
355 the formation of a percolating microfracture by varying both the external state of differential
356 stress and the amount and geometry of initial kerogen patches in shales.

357 **4.2 Microfracture formation by kerogen maturation**

358 Microfracturing in shales involves several steps from the nucleation of microfractures, their
359 propagation, and their final arrest either as a dead end or as a connection to another fracture or
360 a discontinuity such as sedimentary bedding (Chandler et al., 2013). The process of shale
361 maturation and primary migration was reproduced experimentally in recent studies. In a series
362 of laboratory experiments performed on immature shales, the fracturing process was visualized
363 using either scanning electron microscopy (Allan et al., 2014) or time-lapse synchrotron X-ray

364 microtomography (Kobchenko et al., 2011; Panahi et al., 2013; Saif et al., 2016). These
365 experiments show that microfractures initiate in the kerogen patches, where fluids are produced
366 and fluid pressure builds up, and then propagate preferentially along the direction of layering.
367 However, neither confining pressure nor differential stress was applied to these samples during
368 the experiments, and formation of a connected 3D fracture network was not observed.
369 Conversely, the application of a small differential stress is a necessary condition for the
370 formation of vertically oriented microfractures (Figure 4).

371 If fluid is generated within or injected into a spherical cavity in a (hypothetical) homogeneous
372 rock, fracturing is expected to occur in the plane perpendicular to the direction of the
373 (horizontal) far field least principal compressive stress, when the fluid pressure becomes large
374 enough. However, fluid producing kerogen and clay mineral flakes, oriented preferentially
375 along the bedding plane, constitute weak microstructures that act as pre-existing microfractures
376 that propagate along the bedding direction as they are inflated by progressive fluid production.
377 This happens during kerogen maturation that leads to an overall volume increase on the order
378 of 10-20% and a local pressure that may be high enough to fracture source rocks (Pelet and
379 Tissot, 1971; Vernik, 1994; Hunt, 1990; Capuano, 1993; Vernik, 1994; Jin et al., 2010). The
380 anisotropic rock strength, also a consequence of the orientation of strongly anisometric kerogen
381 flakes and inorganic mineral grains, also favors fracture growth along the bedding plane (e.g.
382 Keller et al. 2011; Harrington and Horseman, 1999). Some microfractures may nucleate along
383 directions that are inclined at large angles relative to the bedding plane, and fractures that are
384 propagating in the direction of the bedding plane may be diverted by heterogeneity. For
385 example, while high aspect ratio kerogen flakes, which are typically oriented along the bedding
386 plane, favor horizontal microfractures, low aspect ratio flakes favor vertical fractures (Ozkaya,
387 1998; Lash and Engelder, 2005). Although relatively few in number, vertical growth of these
388 fractures is favored by the far field stress, and they may become large enough to connect many
389 horizontal microfractures leading to the formation of a 3D fracture network that enables fluid
390 flow on the scale of a sedimentary layer, which would further facilitate hydrocarbon primary
391 migration (Fan et al., 2012). This effect of a small differential stress on fracture network growth
392 in 3D is shown both in our experiments (Figure 4) and in the numerical simulations (Figures 10
393 and 11).

394 **4.3 Dynamics of microfractures during primary migration**

Analogue experiments have been performed using transparent brittle hydrogels that enable optical characterization of the fracturing dynamics driven by internal gas production (Bons and van Milligen, 2001; Kobchenko et al., 2013, 2014; Zanella et al., 2014). In these systems, CO_2-producing yeast was mixed into a brittle solid (i. e. the gel). With gas production, microfractures nucleate in the elastic solid and then propagate, leading to the formation of a well-developed fracture network that facilitates gas expulsion. Several results relevant to the development of conceptual models for shale maturation and fluid expulsion emerged from these experiments. Firstly, the fracture network has geometrical and topological properties that are intermediate between those of two end-member drainage networks found in nature, namely river systems and hierarchical fracture networks (Kobchenko et al., 2013). Secondly, these experiments show that gas expulsion and fracture opening and closing are intermittent, and that the fractures close once all the gas has been produced in the solid and escaped from it. Moreover, the dynamics of individual fracture opening and closing are rather complex, with a power-law gas volume fluctuation spectrum, due to the long-range elastic interactions in the solid (Bons and van Milligen, 2001, Kobchenko et al., 2014). These experiments show that the microfracturing process is controlled by several parameters, including the amount of fluid produced during maturation, the kinetics of maturation, the permeability and elastic parameters of the solid and the thickness of the elastic layer in which fluids are produced. These experiments also show that once the fractures formed, they may close completely when the produced fluid has escaped, leaving behind well-defined low-cohesion interfaces, which may heal or cement over time. Making an analogy with shales, microfractures therefore appear to form during maturation and then close. When closed, their transport properties are similar to those of the shale matrix or depend on local cementation. However, if the fluid pressure increases, they can be preferentially reopened, providing pathways for fluid transport.

Our results show that the state of stress in shales during maturation and the initial geometry of the kerogen patches control the final geometry of the microfractures produced. Importantly, the presence of a differential stress, even small, is enough to produce a network of fractures percolating in 3D. At zero differential stress, the final geometry is controlled by the layers where kerogen is concentrated and microfractures are mainly bed parallel. Under the effect of a moderate differential stress, microfractures development is controlled by the external loading and initial kerogen patches distribution with the microfractures being oriented both horizontally and along the direction of the main compressive stress.

To summarize, in organic-rich immature shales, patches of kerogen are disseminated in the matrix along preferential beds and are oriented parallel to sedimentary layering. With maturation, the organic matter decomposes, increases locally the fluid pressure, and produces oil and gas that escape through the formation of horizontal and vertical microfractures. A fracture network forms when horizontal and vertical microfractures cross-cut in 3D and create a percolating flow path, allowing primary migration (Figure 13). The initial geometry of the patches, their density in the matrix, and the external stress control the final geometry of the fracture network. The local stresses due to fluid overpressure interact with the external stresses applied on the medium. Depending on these interactions, the microfractures may be oriented mainly parallel to the bedding (low differential stress, large kerogen patches), perpendicular to it (high vertical stress) or form a 3D network that percolates through the entire volume.

5. Conclusion

The influence of external and internal parameters on the microfracturing of immature shales is investigated here through a coupled experimental and numerical approach. Green River shales were heated until the organic matter they contain matured and produced hydrocarbon that escaped by fracturing the matrix. In the presence of a small differential stress, both bed-parallel and bed-perpendicular fractures form, creating a percolating network in three dimensions. Discrete element numerical simulations show that, at constant temperature, the controlling parameters are the initial geometry of the kerogen patches and the state of external stress. The main results are:

1) Due to their preferential orientation, kerogen patches tend to favor initial fracturing in directions parallel to bedding;
2) In the presence of a differential stress, with the vertical compressive stress larger than the horizontal stresses, vertical fractures can develop.
3) The density of microfractures depends on initial kerogen composition and external stress.
4) The conditions under which a percolating network of fractures is formed, allowing fluid escape and primary migration are identified and it is shown that the presence of a differential stress is necessary, and that an initial configuration where kerogen patches are organized in several layers is necessary to connect vertically microfractures and allow fluid expulsion.

Acknowledgements

This work was supported by a research fellowship of CNPq to MGT and the 2013 AGIR programme of the University Grenoble Alpes. We thank Elodie Boller at the beamline ID19 of the European Synchrotron Radiation Facility in Grenoble (data in Figure 1) and Pascal Charrier and Jacques Desrues at the Laboratoire 3S-R, UMR 5521 CNRS, Univ. Grenoble Alpes for the laboratory tomograph acquisitions (data in Figures 4 and 13).

References

Ababou, R., Valera, I. C., and Poutrel, A. (2011). Macro-permeability distribution and anisotropy in a 3D fissured and fractured clay rock: excavation damaged zone around a cylindrical drift in Callovo-Oxfordian Argilite (Bure). Physics and Chemistry of the Earth, 36, 1932–1948.

Abousleiman, Y. N., Tran, M. H., and Hoang, S. (2008). Laboratory characterization of anisotropy and fluid effects on shale mechanical properties using inclined direct shear testing device IDSTD. In *The 42nd US Rock Mechanics Symposium (USRMS)*. American Rock Mechanics Association.

Allan, A. M., Vanorio, T., and Dahl, J. E. (2014). Pyrolysis-induced P-wave velocity anisotropy in organic-rich shales. Geophysics, 79(2), D41-D53.

Bolton, A. J., Maltman, A. J., and Fisher, Q. (2000). Anisotropic permeability and bimodal pore-size distributions of fine-grained marine sediments. Marine and Petroleum Geology, 17, 657-672.

Bons, P. D., and B. P. van Milligen (2001). New experiment to model self-organized critical transport and accumulation of melt and hydrocarbons from their source rocks, Geology, 29, 919-922.

Brantut, N., Schubnel, A., Rouzaud, J. N., Brunet, F., and Shimamoto, T. (2008). High-velocity frictional properties of a clay-bearing fault gouge and implications for earthquake mechanics. Journal of Geophysical Research: Solid Earth, 113(B10).

485 Brantut, N., Schubnel, A., David, E. C., Héripré, E., Gueguen, Y., and Dimanov, A. (2012).
486 Dehydration-induced damage and deformation in gypsum and implications for subduction zone
487 processes. Journal of Geophysical Research: Solid Earth, 117(B3), B03205.

488 Breyer, J. (2012). Shale Reservoirs: Giant Resources for the 21st Century, AAPG Memoir 97
489 (Vol. 97). AAPG.

490 Capuano, R. M. (1993). Evidence of fluid flow in microcracks in geopressured shales. AAPG
491 Bulletin, 77, 1303–1314.

492 Catalano, E., Chareyre, B., and Barthélemy, E. (2014). Pore-scale modeling of fluid-particles
493 interaction and emerging poromechanical effects. International Journal for Numerical and
494 Analytical Methods in Geomechanics, 38, 51-71.

495 Chandler, M. R., P. G. Meredith, and Crawford, B. R. (2013). Experimental determination of
496 the fracture toughness and ductility of the Mancos Shale, Utah. *75th EAGE Conference &*
497 *Exhibition incorporating SPE EUROPEC 2013*.

498 Chareyre, B., Cortis, A., Catalano, E., and Barthélemy, E. (2012). Pore-scale modeling of
499 viscous flow and induced forces in dense sphere packings. Transport in porous media, 94, 595-
500 615.

501 Dewhurst, D.N., A.F. Siggins, J. Sarout, M. Raven and H.M. Nordgard-Bolas (2011).
502 Geomechanical and ultrasonic characterization of a Norwegian Sea shale. Geophysics 76,
503 WA101–WA111.

504 Duriez, J., Scholtès, L., & Donzé, F. V. (2016). Micromechanics of wing crack propagation for
505 different flaw properties. Engineering Fracture Mechanics, 153, 378-398.

506 Cundall P. A., and Strack O. D. L. (1979). A discrete numerical model for granular assemblies.
507 Geotechnique, 29, 47–65.

508 England, W. A., Mackenzie, A. S., Mann, D. M., and Quigley, T. M. (1987). The movement
509 and entrapment of petroleum fluids in the subsurface. Journal of the Geological Society, 144,
510 327-347.

511 Fan, Q., Jin, Z. H. and Johnson, S. E (2012). Modelling petroleum migration through
512 microcrack propagation in transversely isotropic source rocks. Geophysical Journal
513 International, 190, 179–187, doi: 10.1111/j.1365-246X.2012.05516.x.

514 Gale, J. F., Laubach, S. E., Olson, J. E., Eichhubl, P., and Fall, A. (2014). Natural fractures in
515 shale: A review and new observations. AAPG Bulletin, 98, 2165-2216.

516 Ghayaza, M., Skoczylas, F., Robinet, J., and Talandier, J. (2013). Self-sealing capacity of
517 macro-cracked argillite under confinement. Poromechanics V, 1580-1589, doi:
518 10.1061/9780784412992.187.

519 Harrington, J. F., and S. T. Horseman (1999). Gas transport properties of clays and mudrocks.
520 Geological Society, London, Special Publications, 158(1), 107-124.

521 Holland, M., Urai, J. L., van der Zee, W., Stanjek, H., and Konstanty, J. (2006). Fault gouge
522 evolution in highly overconsolidated claystones. Journal of Structural Geology, 28, 323-332.

523 Horsrud, P., E.F. Sønstebø and R. Bøe (1998). Mechanical and petrophysical properties of
524 North Sea shales. International Journal of Rock Mechanics and Mining Sciences, 35, 1009-
525 1020.

526 Hunt, J.M., 1996. Petroleum Geochemistry and Geology, second ed., New York.

527 Jamtveit, B., Austrheim, H., and Malthe-Sørenssen, A. (2000). Accelerated hydration of the
528 Earth's deep crust induced by stress perturbations. Nature, 408, 75-78.

529 Jamtveit, B., and Hammer, O. (2012) Sculpting of rocks by reactive fluids, Geochemical
530 Perspectives, 1(3), 341-477.

531 Jin, Z. H., Johnson, S. E., and Fan, Z. Q. (2010). Subcritical propagation and coalescence of
532 oil-filled cracks: Getting the oil out of low-permeability source rocks. Geophysical Research
533 Letters, 37,,L01305, doi:10.1029/2009GL041576.

534 Kalani, M., Jahren, J., Mondol, N. H., & Faleide, J. I. (2015). Petrophysical implications of
535 source rock microfracturing. International Journal of Coal Geology, 143, 43-67.

Keller, L.M., L. Holzer, R. Wepf and P. Gasser (2011). 3D geometry and topology of pore pathways in Opalinus clay: Implications for mass transport. Applied Clay Science 52, 85-95.

Kobchenko, M., Panahi, H., Renard, F., Dysthe, D. K., Malthe-Sorrenssen, A., Mazzini, A., Scheibert, J. Jamtveit, B., and Meakin P. (2011). 4D imaging of fracturing in organic-rich shales during heating. Journal of Geophysical Research, 116, B12201, doi:10.1029/2011JB008565.

Kobchenko, M., Hafver, A., Jettestuen, E., Renard, F., Galland, O., Jamtveit, B., and Dysthe, D. (2014). Evolution of a fracture network in an elastic medium with internal fluid generation and expulsion. Phys. Rev. E, 90, 052801.

Kozicki, J., and Donzé, F. V. (2008). A new open-source software developed for numerical simulations using discrete modeling methods. Computer Methods in Applied Mechanics and Engineering, 197, 4429-4443.

Kozicki, J., and Donzé, F. V. (2009). Yade-open DEM: an open-source software using a discrete element method to simulate granular material. Engineering Computations, 26, 786-805.

Kranz, R.L., 1983. Microcracks in rocks: A review. Tectonophysics, 100, 449-480.

Lafargue, W., Espitalie, J., Broks, T. M., and Nyland, B. (1994). Experimental simulation of primary migration. Organic geochemistry, 22, 575-586.

Lafargue, E., Marquis, F., and Pillot, D. (1998). Rock-Eval 6 applications in hydrocarbon exploration, production, and soil contamination studies. Revue de l'institut français du pétrole, 53, 421-437.

Lash, G. G., and Engelder, T. (2005). An analysis of horizontal microcracking during catagenesis: Example from the Catskill delta complex. AAPG Bulletin, 89, 1433-1449.

Noiriel, C., Renard, F., Doan, M. L., and Gratier, J. P. (2010). Intense fracturing and fracture sealing induced by mineral growth in porous rocks. Chemical Geology, 269, 197-209.

Ougier-Simonin, A., Renard, F., Boehm, C., & Vidal-Gilbert, S. (2016). Microfracturing and microporosity in shales. Earth-Science Reviews, 162, 198-226.

561 Padin, A., A.N. Tutuncu and S. Sonnenberg (2014). On the Mechanisms of Shale Microfracture
562 Propagation. SPE Hydraulic Fracturing Technology Conference, Society of Petroleum
563 Engineers.

564 Panahi, H., Kobchenko, M., Renard, F., Mazzini, A., Scheibert, J., Dysthe, D. K., Jamtveit, B.,
565 and Meakin P. (2013). 4D X-ray tomography imaging of hydrocarbon escape pathway
566 formation in heated organic-rich shales: a proxy for primary migration? SPE Journal,
567 SPE162939, 366-377.

568 Papachristos, E. et al. 2016. 3D hydro-mechanical modeling of multiple injections, 50th ARMA
569 Conference.

570 Peacock, S. M. (1993). Large-scale hydration of the lithosphere above subducting slabs.
571 Chemical Geology, 108, 49-59.

572 Pelet, R., and Tissot, B. (1971). Nouvelles données sur les mécanismes de genèse et de
573 migration du pétrole: simulation mathématique et application à la prospection. In *8th World*
574 *Petroleum Congress*, 13-18 June, Moscow, USSR, 12 pages.

575 Røyne, A., Jamtveit, B., Mathiesen, J., and Malthe-Sørenssen, A. (2008). Controls on rock
576 weathering rates by reaction-induced hierarchical fracturing. Earth and Planetary Science
577 Letters, 275, 364-369.

578 Rudkiewicz, J. L., Brévart, O., Connan, J., and Montel, F. (1994). Primary migration behaviour
579 of hydrocarbons: from laboratory experiments to geological situations through fluid flow
580 models. Organic geochemistry, 22, 631-639.

581 Saffer, D. M., and Bekins, B. A. (1998). Episodic fluid flow in the Nankai accretionary
582 complex: Timescale, geochemistry, flow rates, and fluid budget. Journal of Geophysical
583 Research: Solid Earth, 103, 30351-30370.

584 Saif, T., Lin, Q., Singh, K., Bijeljic, B., & Blunt, M. J. (2016). Dynamic imaging of oil shale
585 pyrolysis using synchrotron X-ray micro-tomography. Geophysical Research Letters, in press.

586 Sarout, J. and Guéguen, Y. (2008). Anisotropy of elastic wave velocities in deformed shales:
587 Part 1-Experimental results. Geophysics, 73, D75-D89.

588 Scholtès, L., and Donzé, F. V. (2012). Modelling progressive failure in fractured rock masses
589 using a 3D discrete element method. International Journal of Rock Mechanics and Mining
590 Sciences, 52, 18-30.

591 Scholtès, L., and Donzé, F. V. (2013). A DEM model for soft and hard rocks: Role of grain
592 interlocking on strength. Journal of the Mechanics and Physics of Solids, 61, 352-369.

593 Skurtveit, E., A. Eyvind, M. Soldal, M. Angeli, and Z. Wang (2012). Experimental investigation
594 of CO_2 breakthrough and flow mechanisms in shale, Petroleum Geoscience, 18, 3-15, doi:
595 10.1144/1354-079311-016.

596 Šmilauer, V. et al. (2015). Reference manual. In Yade Documentation 2nd ed. The Yade
597 Project, DOI 10.5281/zenodo.34045.

598 Snarsky, A. N. (1961). Relationship between primary migration and compaction of rocks.
599 Petroleum Geology: A digest of Russian literature on Petroleum Geology, 5, 362-365.

600 Sone, H., and Zoback, M. D. (2013). Mechanical properties of shale-gas reservoir rocks – Part
601 1: Static and dynamic elastic properties and anisotropy. Geophysics, 78, D381-D392.

602 Ulmer, P., and Trommsdorff, V. (1995). Serpentine stability to mantle depths and subduction-
603 related magmatism. Science, 268, 858-861.

604 Vernik, L. (1994). Hydrocarbon-generation-induced microcracking of source rocks.
605 Geophysics, 59, 555-563.

606 Walsh, J.B. (1965a). The effect of cracks on the compressibility of rock. Journal of Geophysical
607 Research, 70, 381-389.

608 Walsh, J.B. (1965b). The effect of cracks on the uniaxial elastic compression of rocks. Journal
609 of Geophysical Research, 70, 399-411.

610 Walsh, J.B. (1965c). The effect of cracks in rocks on Poisson's ratio. Journal of Geophysical
611 Research, 70, 5249-5257.

612 Yang, Y. and A. C. Aplin (2007). Permeability and petrophysical properties of 30 natural
613 mudstones. Journal of Geophysical Research, 112, B03206, doi:10.1029/2005JB004243.

614 Zanella, A., Cobbold, P. R., & de Veslud, C. L. C. (2014). Physical modelling of chemical
615 compaction, overpressure development, hydraulic fracturing and thrust detachments in organic-
616 rich source rock. Marine and Petroleum Geology, 55, 262-274.

617 Zhang, X., Jeffrey, R. G., & Thiercelin, M. (2008). Escape of fluid-driven fractures from
618 frictional bedding interfaces: a numerical study. Journal of Structural Geology, 30(4), 478-490.

619 Figures and Tables

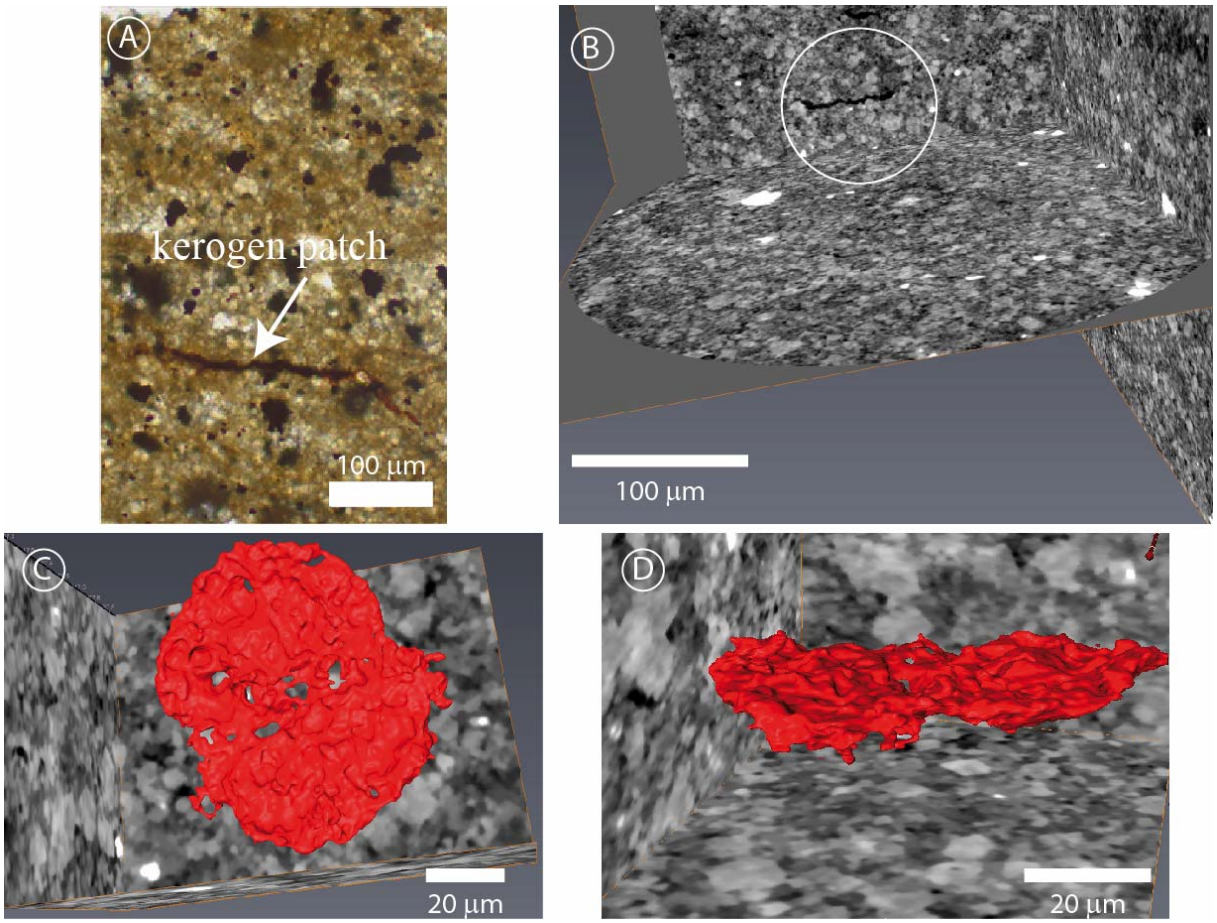

620

621 Figure 1: Imaging of kerogen in a Green River shale sample. A) Optical microscopy showing
622 a kerogen patch. B-D) X-ray microtomography imaging of a Green River shale sample at a
623 voxel size of 0.16 micron showing the microstructure of the shale where the various gray scale
624 levels underline the individual grains (for example pyrite minerals appear in white). A kerogen
625 patch is parallel to bedding (white circle in B). C-D) Zooms on a patch of kerogen which forms
626 an ellipsoid, 70 micrometers wide and 2-4 micrometers height. The outer surface of the bed
627 parallel kerogen patch is colored in red.

628

629 Table 1: Properties of the synthetic shale rock and fluid used in the numerical simulations. UCS:
630 Uniaxial Compressive Strength. UTS: Uniaxial Tensile Strength.

Shale model		Fluid	
Density	2500 kg/m^3	Bulk	2.2E9 Pa
Young's modulus	26x10^9 Pa	Viscosity	10^{-3} Pa s
Poisson's ratio	0.25	Flow rate	10^{-6} m^3/s
UTS	3 MPa		
UCS	25 MPa		
Permeability	$10^{-23}m^2$		

631

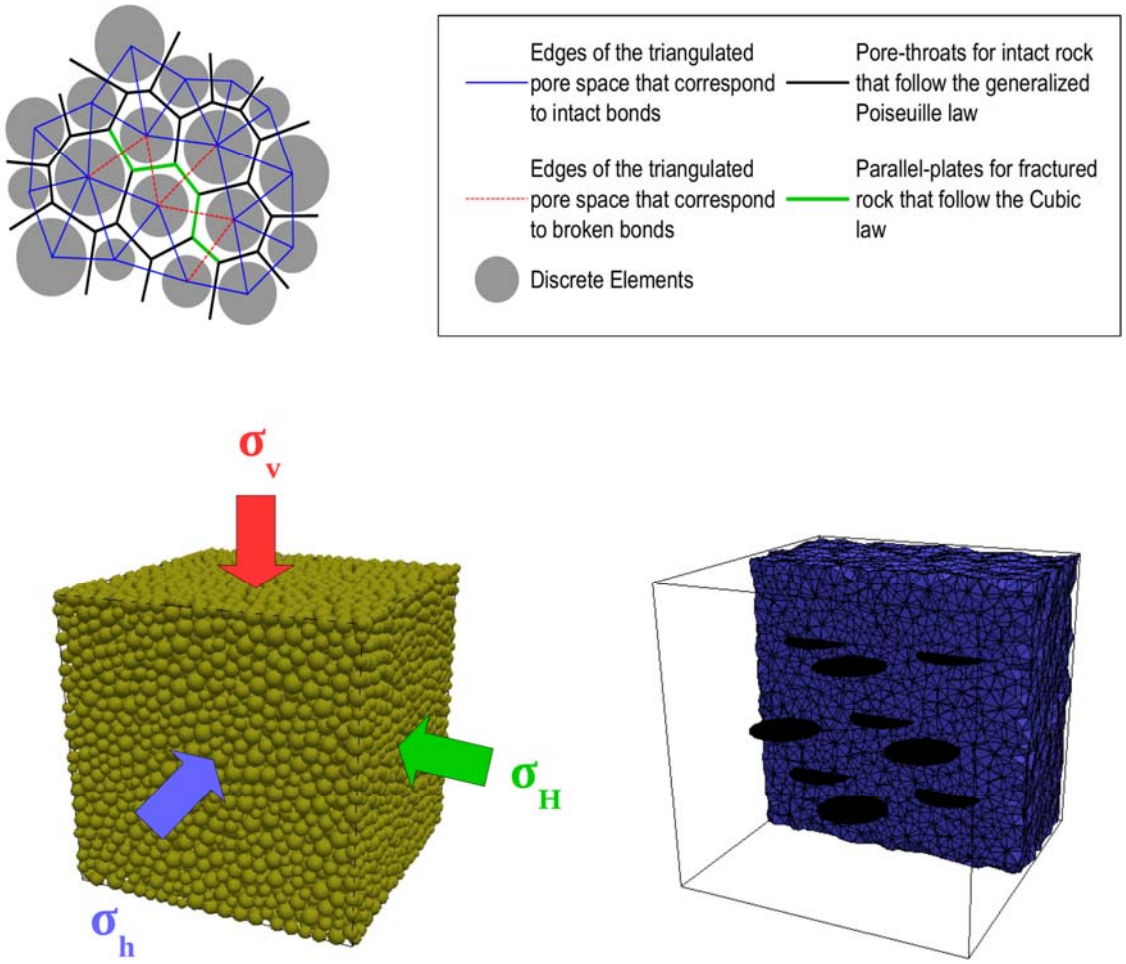

632

633 Figure 2: a) Principles of the numerical model illustrated by a 2D slice sketch. b) 3D view of
634 the shale rock volume with discrete elements and c) the associated finite volume mesh for the
635 fluid with the patches of kerogen represented as black ellipsoids.

636

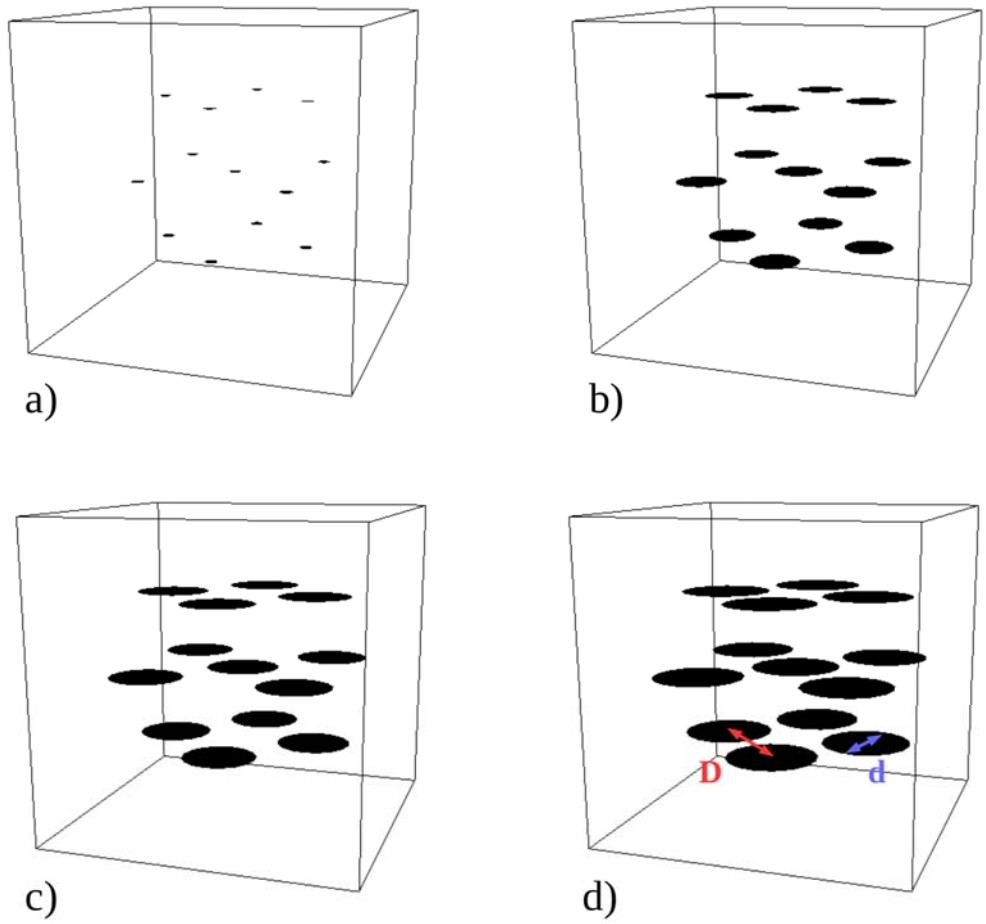

Figure 3: Side-view of the inside of the shale rock that contains patches of kerogen represented as ellipsoids (see Figure 1c-d). The number of patches is initially fixed (here 13) and the persistence $p = d / D$ is varied, where d is the size of each patch and D is the distance between them. Taking D = 8.5 mm, different persistence values can be obtained with a) p = 0.12 (d = 1 mm), b) p = 0.47 (d = 3mm), and c) p = 0.71 (d = 8.5 mm), and d) p = 0.83 (d = 10 mm). In the numerical model the persistence is similar to that in the Green River Shale sample, whereas d and D are ten to hundred times smaller in the natural sample.

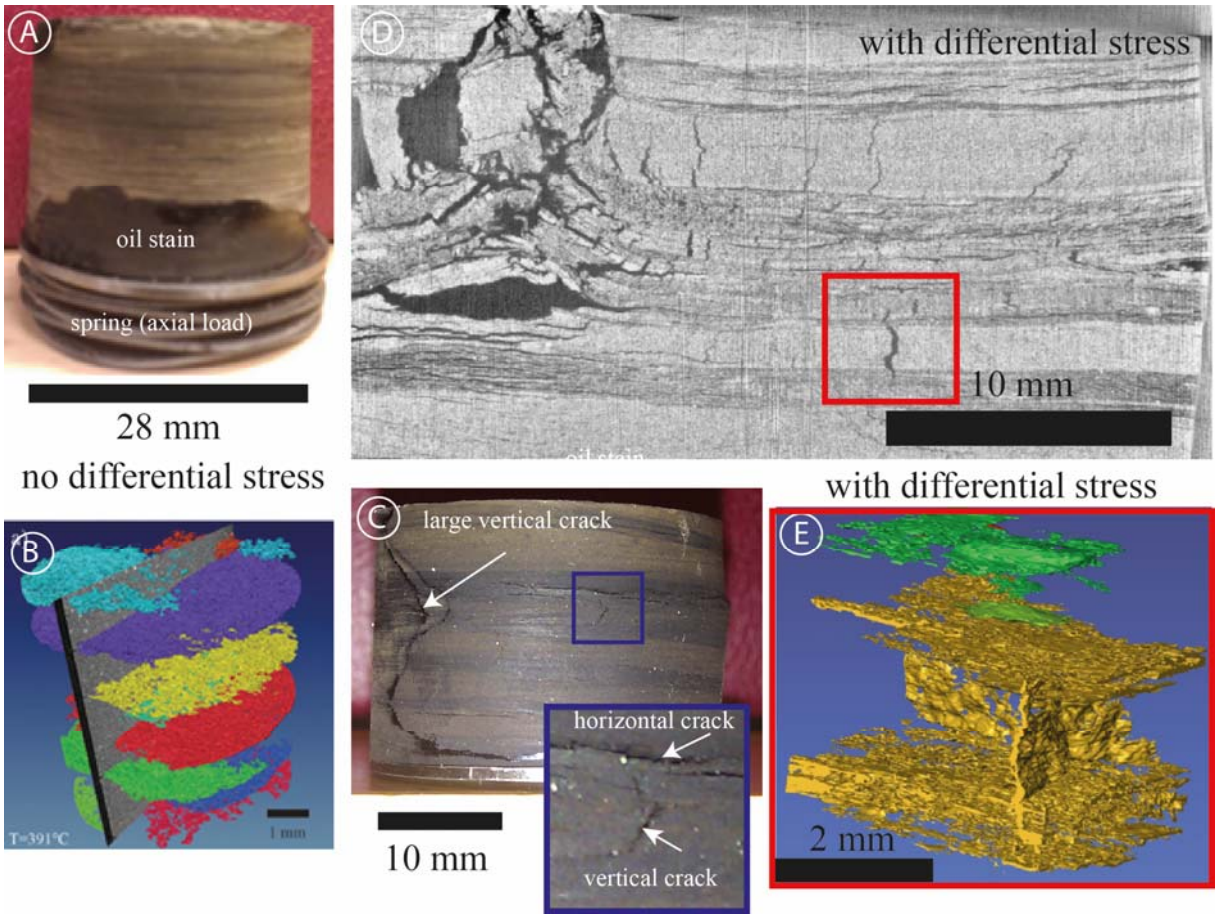

Figure 4: Shale sample after heating at 390°C for 24 hours. A) Sample core sample with the wave spring (at the bottom) that imposed a small differential stress inside the pressure vessel. A stain of hydrocarbon (dark) is visible after maturation. B) Microtomography imaging of fractures in a sample heated at atmospheric pressure (adapted from Kobchenko et al., 2011). C-D) 2D slices from 3D X-ray micromotography data of a sample heated under differential stress after maturation. The initial horizontal bedding and the horizontal and vertical fractures produced by kerogen maturation and hydrocarbon maturation can be seen. E) 3D view of the fracture network with connecting horizontal and vertical fractures.

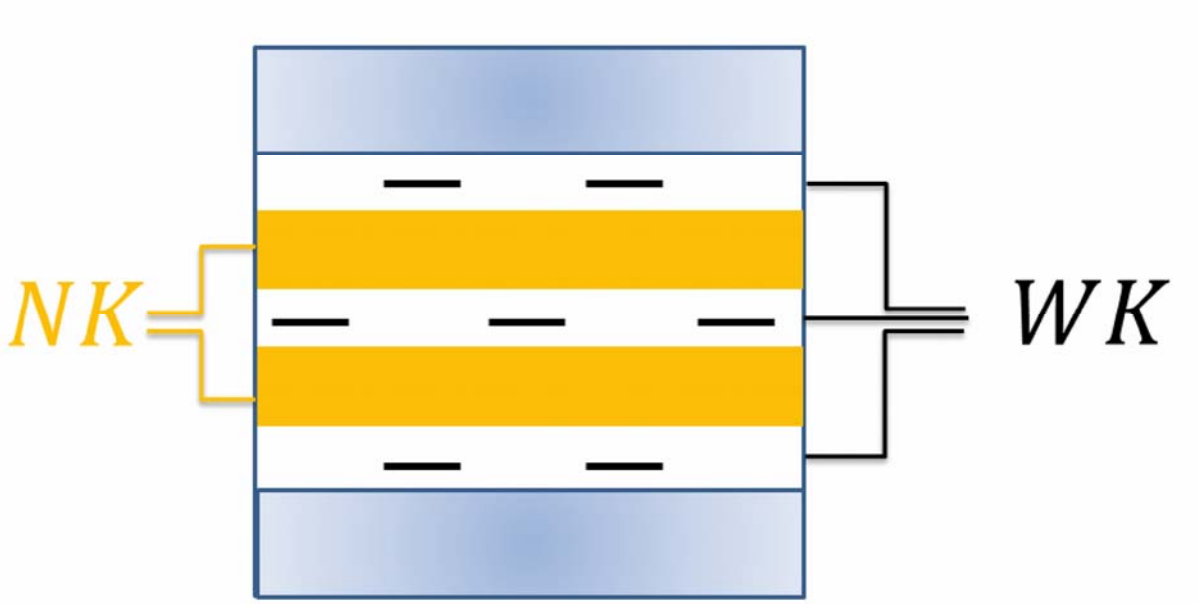

Figure 5: Definition of the parameters NK (kerogen-free layers: *No Kerogen*) and WK (kerogen-rich layers: *With Kerogen*). The surface area of newly created microfractures (parameter P32, see Equation 1) is calculated in kerogen-free and kerogen-rich layers, respectively, and the ratio between these two numbers is called K (see Equation 2).

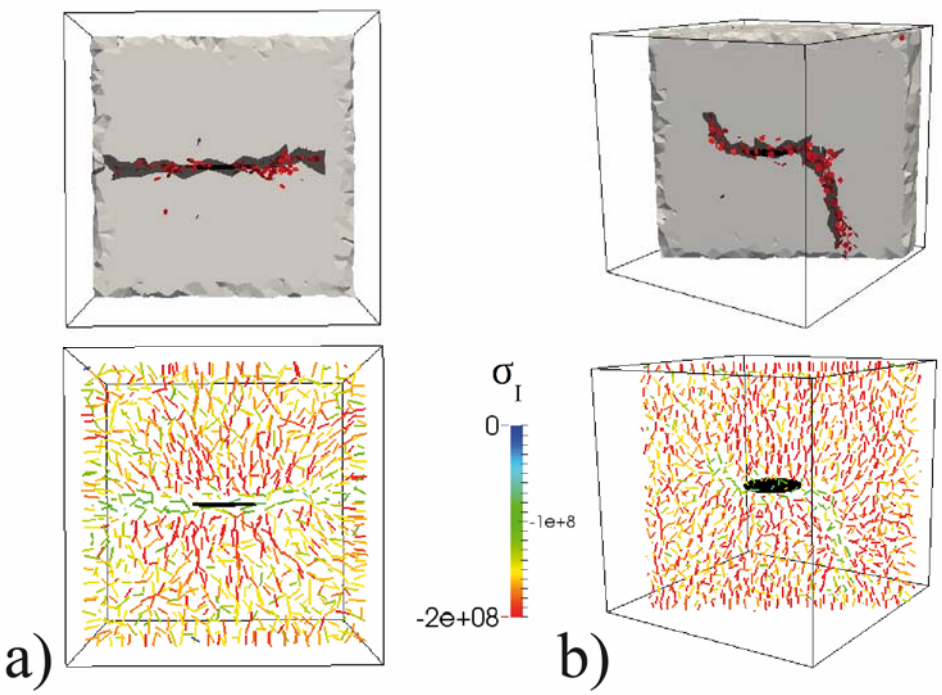

Figure 6: Left side: Slice in the middle of the sample showing microfractures (red discs) and fluid migration (dark gray cells) around a single horizontal kerogen patch for (a) the hydrostatic case with σ_v = 80 MPa and (b) a differential stress of 20 MPa with σ_v = 100 MPa. On the right side, the direction and intensity of local maximum principal stresses σ_1 (Pa) are represented as thin lines colored as a function of their intensity for each case.

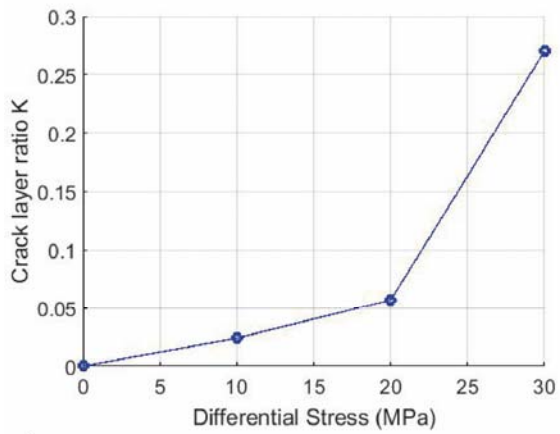

a)

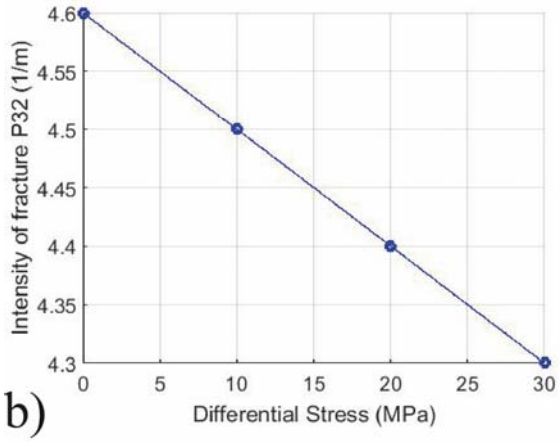

b)

669

670 Figure 7: a) Evolution of the ratio K of microfractures in kerogen-free compared to kerogen-
671 rich layers. b) Intensity of fracturing (parameter P32, see Equation 1) versus differential stress.

672

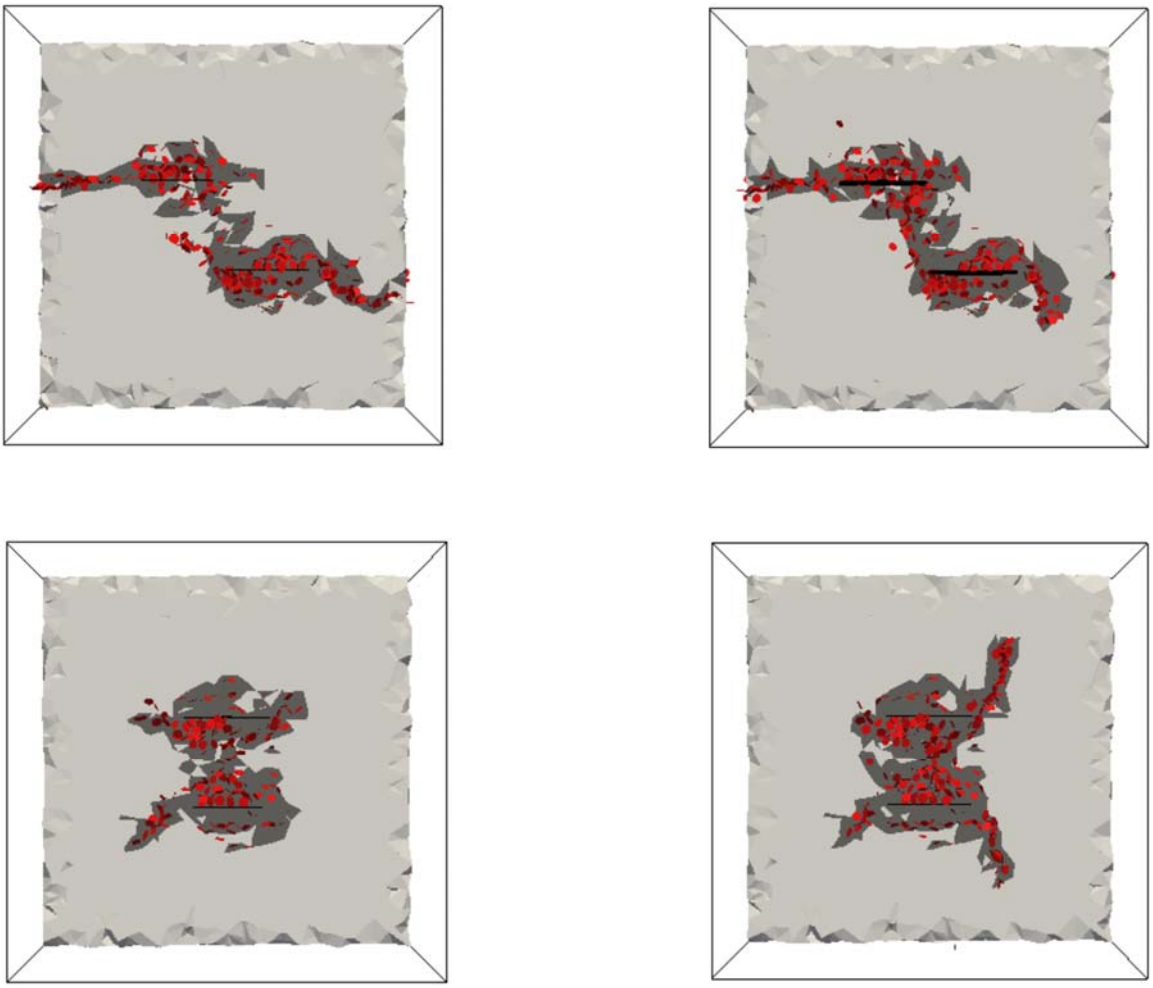

Figure 8: Slice in the middle of the sample showing microfractures (red discs) and fluid migration (dark cells) for (left) hydrostatic loading with σ_v = 80 MPa and (right) a differential stress of 20 MPa with σ_v = 100 MPa for two kerogen patches with relative vertical offsets L = 0 (top) and L = -2r (bottom), where L represents the vertical offset between the two fractures.

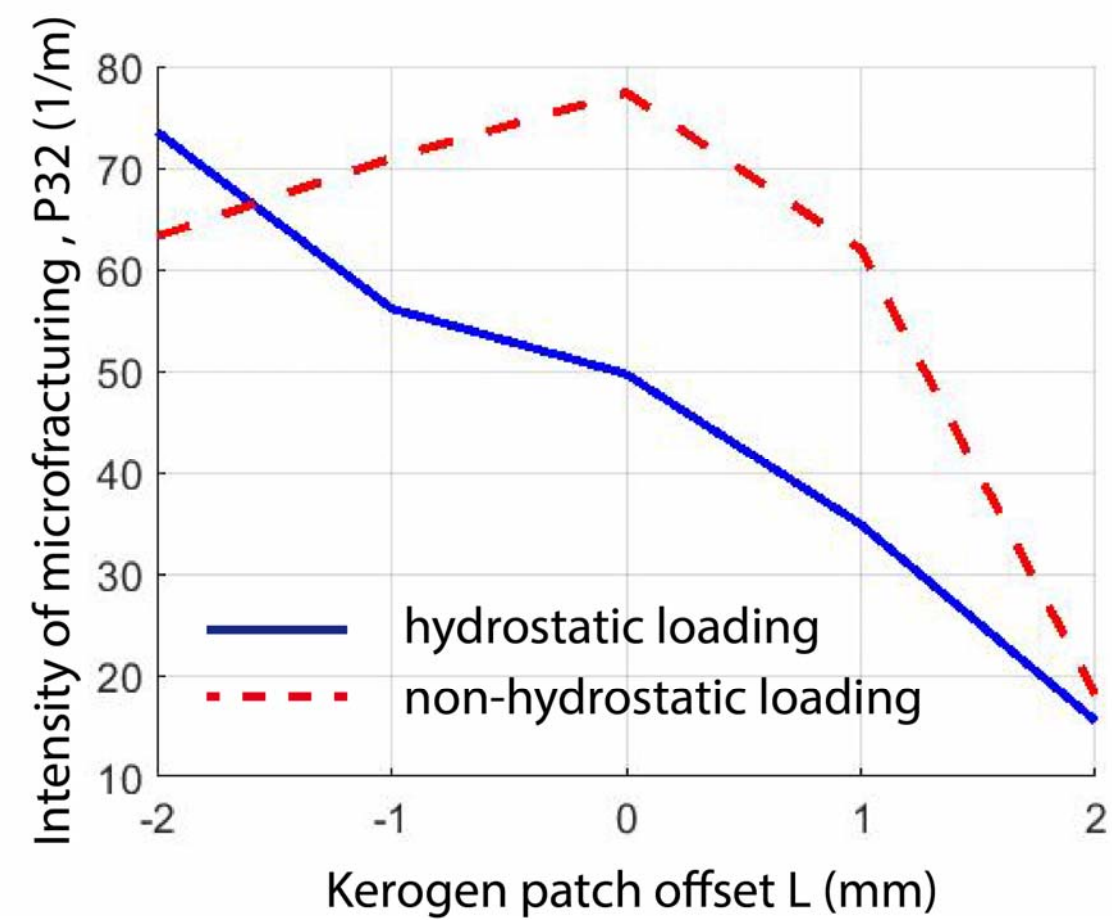

679

680 Figure 9: Intensity of microfracturing (parameter P32, see Eq. 1) versus kerogen patch offset
681 for hydrostatic loading σ_v = 80 MPa (blue line) and differential-stress loading, σ_v = 100 MPa
682 (red dashed line).

683

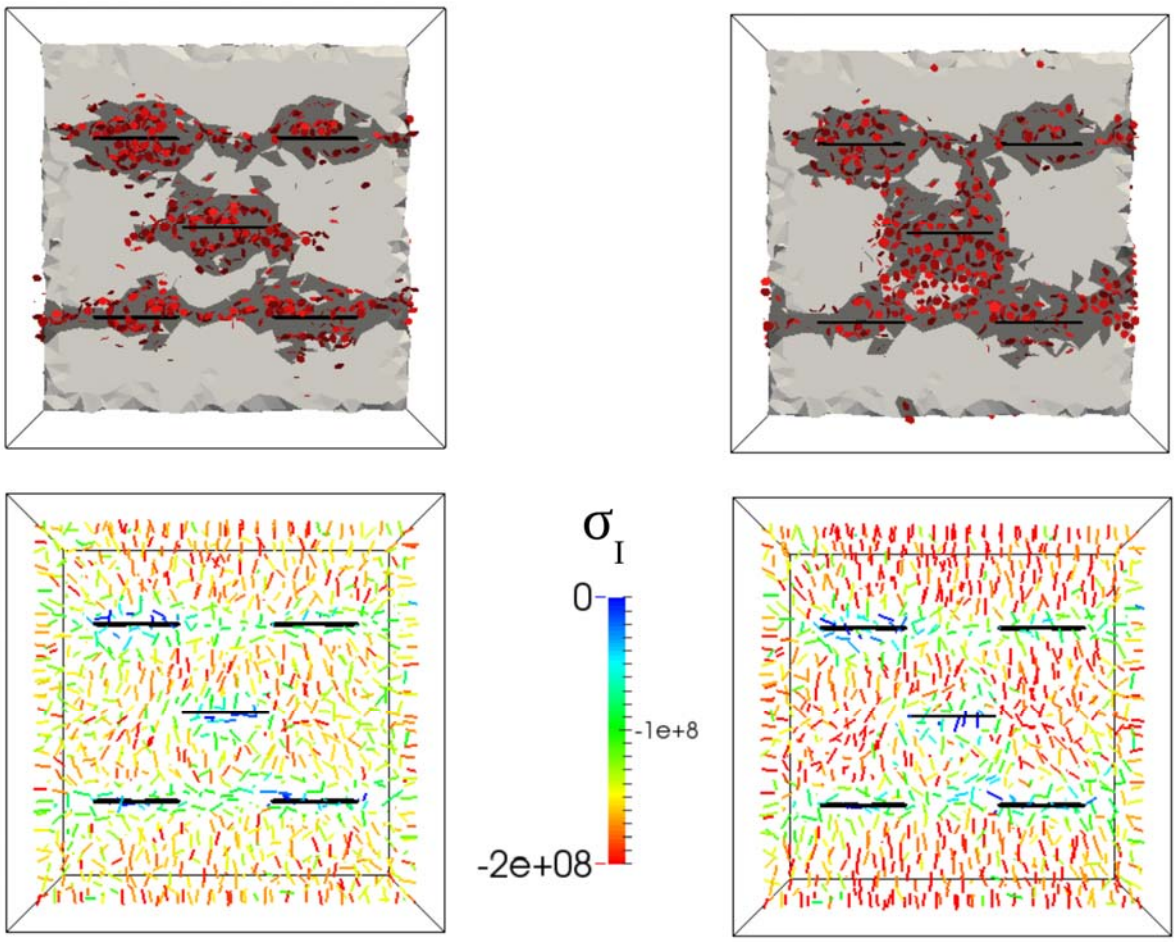

Figure 10: (top) Slice in the middle of the sample showing microfractures (red discs) and fluid migration (dark cells) around thirteen horizontal kerogen patches for (left) the hydrostatic case with σ_v = 80 MPa and (right) a differential stress of 20 MPa with σ_v = 100 MPa. (bottom) The direction and intensity of local maximum principal stress σ_1 (Pa) are represented as thin lines colored as a function of their intensity for each case.

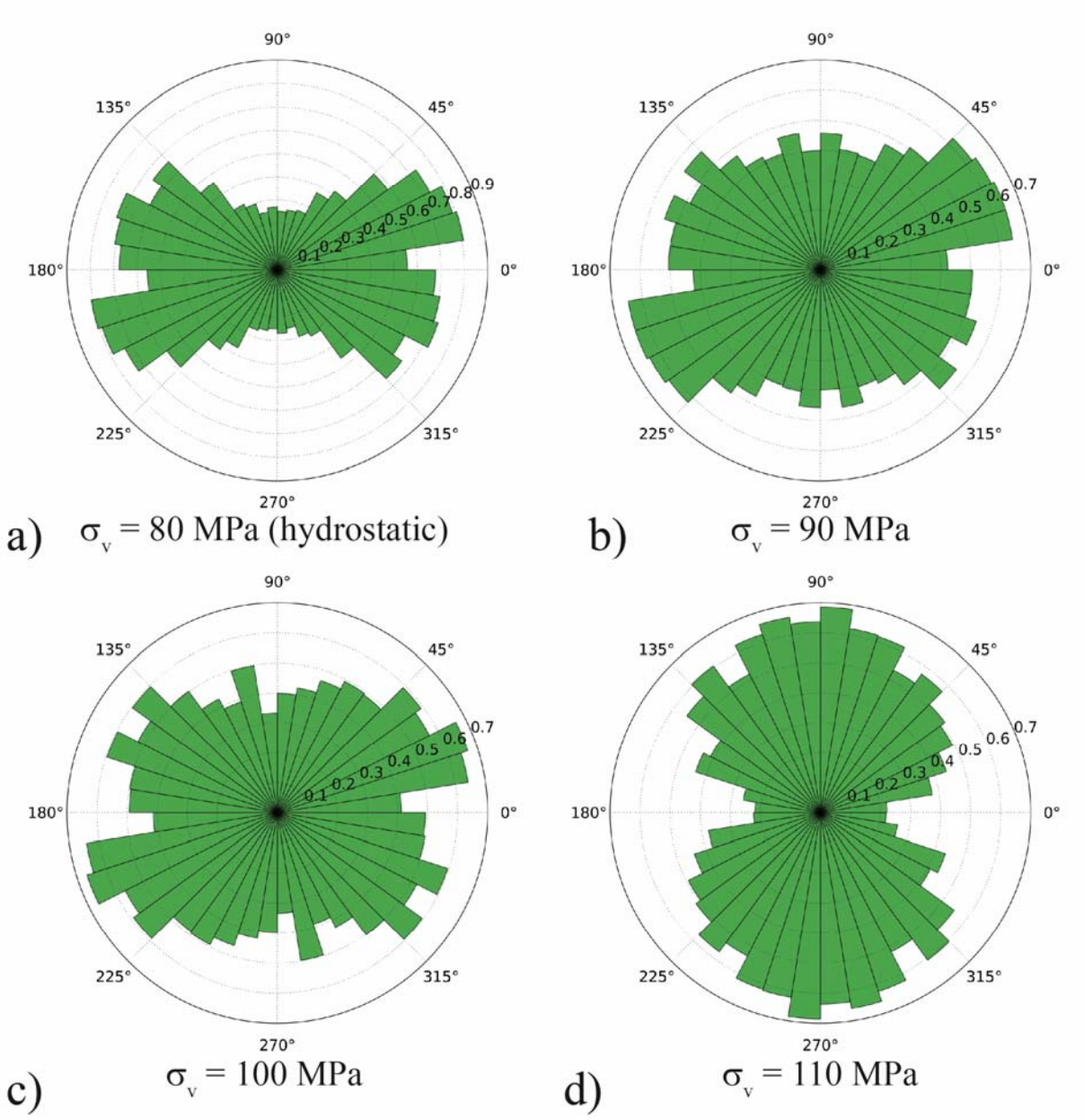

691

692 Figure 11: Normal vector angle of microfractures obtained for simulations with thirteen
693 kerogen patches. a) σ_v = 80 MPa (hydrostatic loading); b) σ_v = 90 MPa; c) σ_v = 100 MPa; d)
694 σ_v = 110 MPa. In all simulations the two horizontal principle stresses are equal to 80 MPa.

695

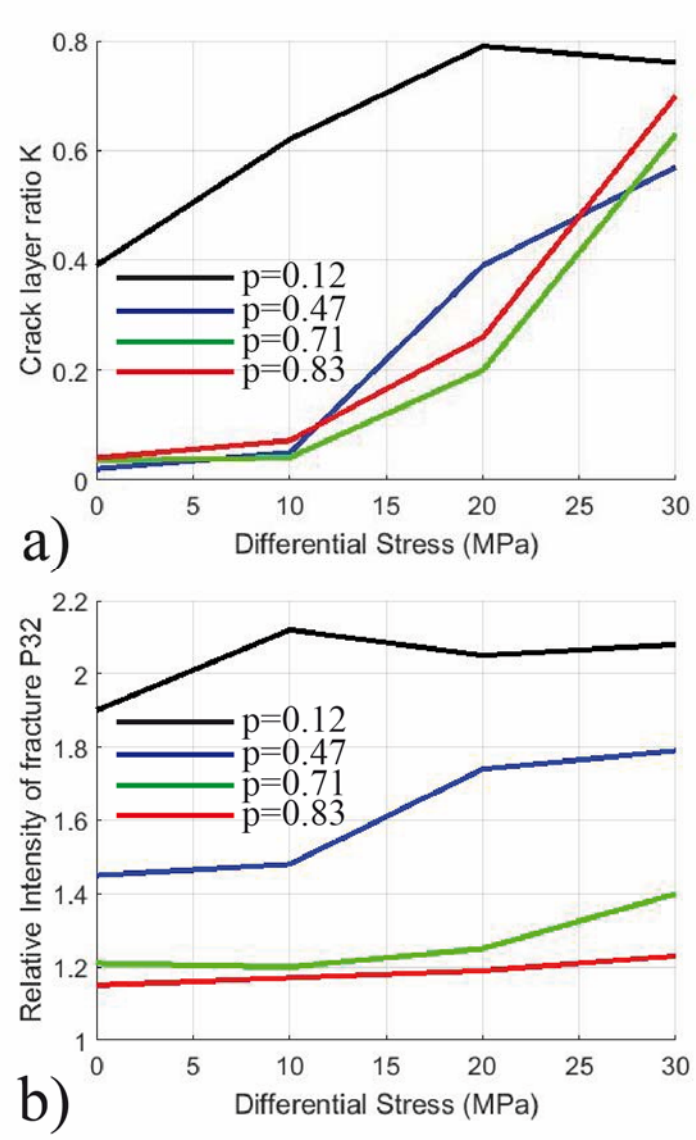

Figure 12: a) Evolution of the ratio of damage K between kerogen-free and kerogen-rich layers (see Eq. 2) versus differential stress for different values of the persistence *p*. b) Evolution of microfracturing intensity (parameter P32, see Eq. 1) versus differential stress for several values of the persistence *p*.

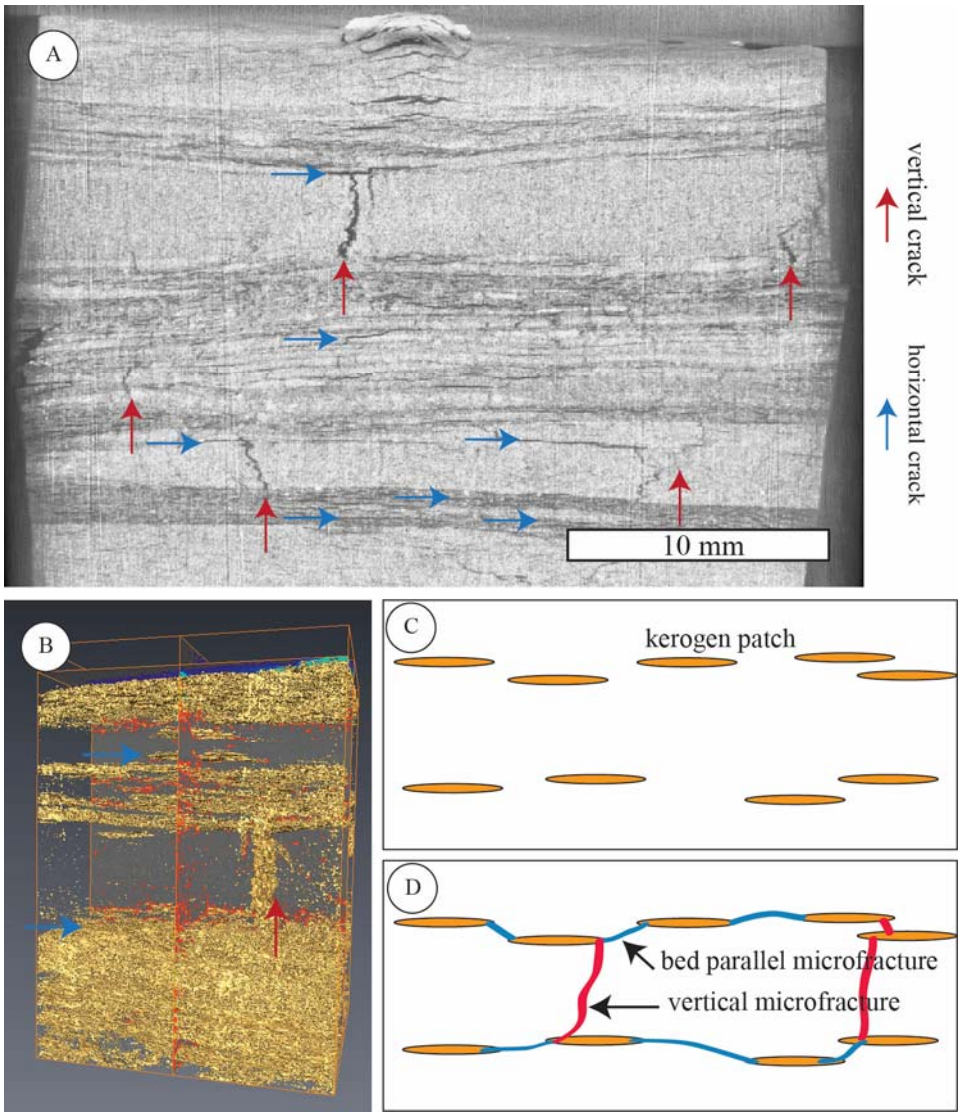

Figure 13: a-b) Microtomography views of a shale sample after maturation at 390°C and differential stress for 24 hours in laboratory conditions. Bed parallel (blue arrows) and bed perpendicular microfractures (red arrows) for a 3D percolating network. c-d) Conceptual diagram of the development of a 3D microfracture network and damage creation by the maturation of organic matter in shales.